Downloaded from orbit.dtu.dk on: May 05, 2023

DTU Library

The Bistatic Sodar "Heimdall", You blow, I listen

Mikkelsen, Torben; Ejsing Jørgensen, Hans; Kristensen, Leif

Publication date:
2007

Document Version
Publisher's PDF, also known as Version of record

Link back to DTU Orbit

Citation (APA):
Mikkelsen, T., Ejsing Jørgensen, H., & Kristensen, L. (2007). *The Bistatic Sodar "Heimdall", You blow, I listen*. Risø National Laboratory. Denmark. Forskningscenter Risoe. Risoe-R No. 1424(EN)

General rights
Copyright and moral rights for the publications made accessible in the public portal are retained by the authors and/or other copyright owners and it is a condition of accessing publications that users recognise and abide by the legal requirements associated with these rights.

- Users may download and print one copy of any publication from the public portal for the purpose of private study or research.
- You may not further distribute the material or use it for any profit-making activity or commercial gain
- You may freely distribute the URL identifying the publication in the public portal

If you believe that this document breaches copyright please contact us providing details, and we will remove access to the work immediately and investigate your claim.

Risø-R-Report

The Bistatic Sodar “Heimdall"

You blow, I listen

Torben Mikkelsen, Hans E. Jørgensen, and Leif Kristensen

Risø-R-1424(EN)

Risø National Laboratory
Technical University of Denmark
Roskilde, Denmark
November 2007

Author: Torben Mikkelsen, Hans E. Jørgensen, and Leif Kristensen
Title: The Bistatic Sodar "Heimdall", You blow, I listen
Department: Wind Energy Department

Risø-R-1424(EN)
November 2007

Abstract (max. 2000 char.):

With the increased exploitation of wind energy, remote sensing of wind profiles in the atmospheric boundary layer has come in focus as an attractive alternative to the operation of tall instrumented masts for wind energy siting and assessment studies. Project "Heimdall" describes a recent feasibility study conducted at Risø in the peiod 2001-2003 of the investigation of a new continuous wave (CW) bistatic sodar, initiated with the aim of investigating and improving the measuring accuracy of sodar remote sensing at heights ranging between 50 and 150 meters, during the often strong wind conditions in a neutrally stratified atmospheric conditions, characteristic for wind energy applications. Here we first describe the theoretical developments for sound wave scattering theory within a bistatic configuration. We calculate the Doppler shifts and returned power for the proposed new Heimdall bistatic configuration, implemented for measurements at 60 meters height above the ground. The bistatic "Heimdall" sodar was subsequently built and set in operation adjacent to the 123 meter tall met tower at Risø National Laboratory, which we had equipped with a sonic reference anemometer installed at the 60 meters height. "Heimdall" measured CW Doppler shifts, subsequently processed into wind speed in real time, along with received power which have been compared with our predictions, and we found that: 1) Our suggested bi-static configuration enabled real-time tracing of the wind speeds with data rates of ~1 Hz from fast processing of the measured spectral measurements of the Doppler shift with an adequate signal-to-noise ratio, and 2) the amplitudes of the measured return powers compared to the predictions within about -10 dB. We conclude that the proposed bi-static configuration provides significantly improved signal-to-noise advantages over similar mono-static configurations, and thereby also better data availability rates for wind speed measurements during strong wind conditions.

ISSN 0106-2840
ISBN 87–550–3250–8

Contract no.:

26-01-0086

Group's own reg. no.:
(Føniks PSP-element)
1130 401--1

Sponsorship:
Danish Technical Research Council

Cover :

"Heimdall" bistatic sodar at Risø.

Pages: 30
Tables: 1
Illustrations: 22
References: 13

Information Service Department
Risø National Laboratory
Technical University of Denmark
P.O.Box 49
DK-4000 Roskilde
Denmark
Telephone +45 46774004
bibl@risoe.dk
Fax +45 46774013
www.risoe.dk

Contents

1 Prologue

A prototype of a bistatic sodar (Sound Detection and Ranging), "Heimdall"[†], has been developed. Here we present the essential part of the theory for sodar anemometry. This is followed by a technical presentation of the Heimdall sodar and some preliminary experimental observations.

There is a vast amount of literature about sodars (Sound Detection and Ranging). There are many types and they are used to measure turbulence characteristics and wind velocities in the atmospheric surface layer. The most common sodar has a monostatic configuration where the transmitter and receiver are the same (You blow and listen). In the bistatic configuration the transmitter and receiver are not the same (You blow and I listen); they are displaced horizontally. The two measuring principles are illustrated in Fig. 1

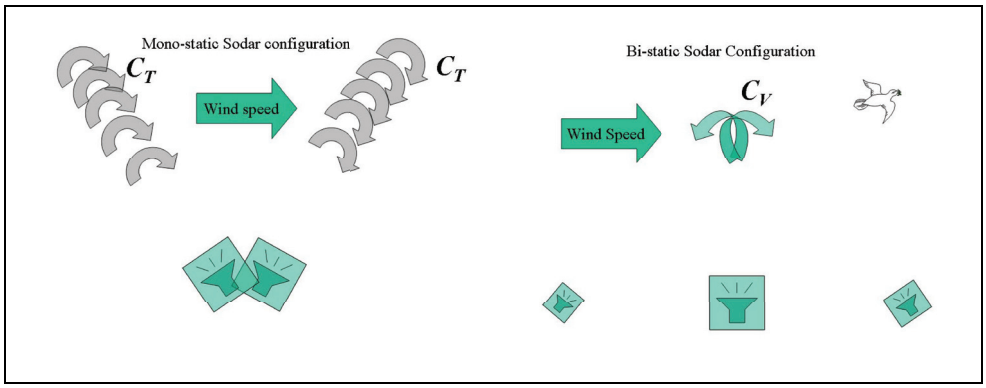

Figure 1. Sketches of a monostatic configuration (left) and a bistatic configuration (right). In the first configuration the sound pulse is Doppler shifted by temperature fluctuations, characterized by the turbulence strength parameter C_T and backscattered 180°*, i.e. the transmitters are also receivers. By sending sound pulses in three directions the mean-wind speed can be determined if horizontal homogeneity is assumed. This is in contrast to the bistatic configuration sodar where the wind speed component in the plane of the transmitting bean and the reflected is determined in the intersecting volumes of the two antenna directivities. In this case the signal strength is enhanced because both temperature fluctuations and the velocity fluctuations with the strength parameter C_V are scattering agents. With two antenna pairs pointing into the same volume it is possible to measure continuously the mean horizontal wind velocity. We might in this case let these two pairs share the same transmitter.*

The switching between transmitting and receiving for the monostatic sodar means that it is impossible to operate it in a continuous mode. For this instrument one duty circle consists of the transmitting a short sound pulse, followed by the receiving of the back-scattered returns. The distance to the traveling sound pulse is monitored by so-called range gating. In other words, a monostatic sodar sound pulse probes—within the maximum range—the atmosphere along the axis of the transmitter/receiver antenna. This is not the case for a bistatic sodar. Here the atmosphere is probed in the rather limited vicinity of the intersection between the axes of the transmitter and the receiver. So far bistatic sodars have been operated

[†]Heimdall is a god in the Norse mythology. He has a lur (war horn). When listening, he can hear the grass grow on the ground and the wool on the sheep.

in the same way as monostatic sodars, but with a bistatic operation it is possible to operate in a continuous mode.

The Doppler shift $\Delta\omega$ can be determined geometrically with the aid of Fig. 2. Consider a plane sound wave with the wave-number vector $\boldsymbol{k}_\circ$ and the frequency $\omega_\circ$ being transmitted from the transmitter T. The scattering eddy is moving with the wind velocity component $\boldsymbol{u}$ in the plane of the two antenna axes and will "feel" that the wave has the frequency

$$\omega = \omega_\circ - \boldsymbol{k}_\circ \cdot \boldsymbol{u}. \tag{1}$$

We assume elastic scattering and the eddy will therefore re-emit a spherical sound wave with the frequency ω. The wave direction towards the receiver R can be characterizes by the wave number $\boldsymbol{k}$, but since the emitter, the eddy, is moving with the velocity $\boldsymbol{u}$ the receiver will "feel" that the frequency is

$$\omega_\mathrm{R} = \omega + \boldsymbol{k} \cdot \boldsymbol{u}. \tag{2}$$

Consequently, the total Doppler shift from transmitter T to receiver R is

$$\Delta\omega \equiv \omega_\mathrm{R} - \omega_\circ = (\boldsymbol{k} - \boldsymbol{k}_\circ) \cdot \boldsymbol{u}. \tag{3}$$

We see that for backscattering

$$\Delta\omega = -2\,\boldsymbol{k}_\circ \cdot \boldsymbol{u}. \tag{4}$$

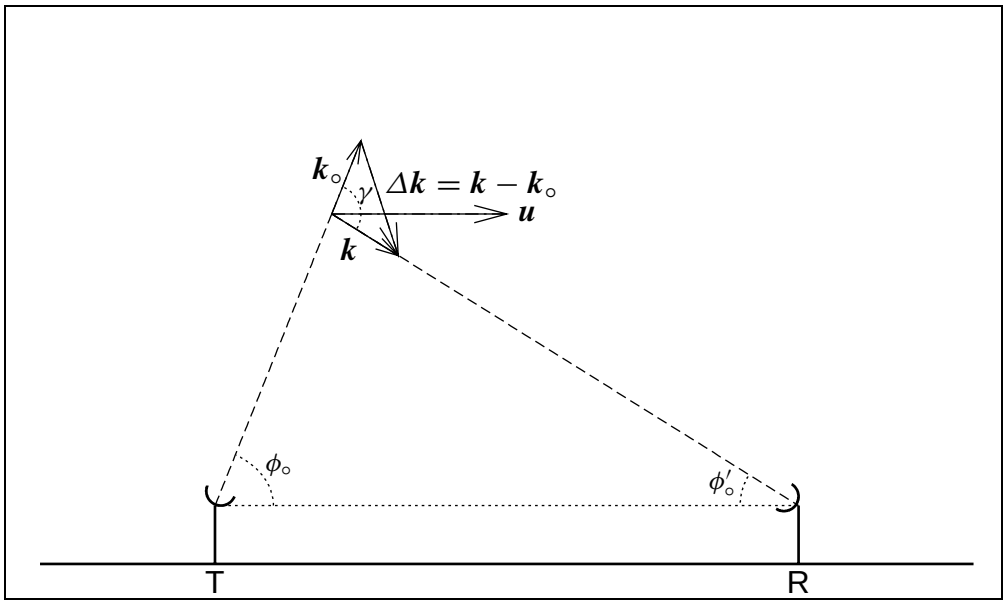

Figure 2. Bistatic configuration. The transmitter T *transmits a plane sound wave with the wave number* $\boldsymbol{k}_\circ$ *with the inclination* $\phi_\circ$ *and the frequency* $\omega_\circ$*. The receiver* R *has the axis inclination* $\phi'_\circ$*. The plane triangle defined by* T, R *and the intersection of the two antenna axes is here assumed vertical. The velocity component in this plane is* $\boldsymbol{u}$*.*

In the following section we discuss some of the theoretical background for the operation of a bistatic sodar for remote anemometry.

2 Theoretical Background

There are three major theoretical subjects of importance, namely sound scattering in the atmosphere, the bistatic sodar equation, and the determination of Doppler shift of the frequency due to the collective part of the motion of the scattering eddies.

2.1 The Cross Section for Sound Scattering

The specific sound scattering cross section, i.e. the total cross section per unit solid angle and volume was derived by Tatarskii (1967). In a notation consistent with Lumley & Panofsky (1964) it can be written

$$\eta(\gamma) = \frac{k^2}{8} \frac{\cos^2(\gamma)}{\sin^2(\gamma/2)} \left\{ \frac{E_T(2k\sin(\gamma/2))}{4T^2} + \frac{E_U(2k\sin(\gamma/2))}{c^2} \cos^2(\gamma/2) \right\}. \quad (5)$$

Here $k = |\boldsymbol{k}|$ is the-wave number of the sound, T and c the overall temperature and velocity of sound, respectively, and γ the scattering angle. The functions $E_T(k)$ and $E_U(k)$ are the energy spectra for temperature and for velocity; they are defined so that when integrated over all wave numbers from zero to infinity the results are the three-dimensional variances of temperature and velocity, respectively.

We want to evaluate (5) in the case of isotropic turbulence where there are simple relations between the energy spectra $E_T(k)$ and $E_U(k)$ and the corresponding one-dimensional spectra $F_T(k)$ and $F_U(k)$ in the direction of the flow [see e.g., (Lumley & Panofsky 1964)]:

$$E_T(k) = -2k \frac{\mathrm{d}F_T}{\mathrm{d}k}, \quad (6)$$

$$E_U(k) = k^3 \frac{\mathrm{d}}{\mathrm{d}k} \left(\frac{1}{k} \frac{\mathrm{d}F_U}{\mathrm{d}k} \right). \quad (7)$$

Let us now consider the one-dimensional spectrum of $\chi(x)$, which could be the streamwise component of the velocity or the temperature. We assume isotropy so $\chi(x)$ is homogeneous with the constant mean value $\langle\chi\rangle$, where angle brackets $\langle\cdot\rangle$ means ensemble averaging. The structure function is defined as

$$D(r) = \left\langle \{\chi(x+r) - \chi(x)\}^2 \right\rangle. \quad (8)$$

The autocovariance function which is more directly related to the spectrum is

$$R(r) = \langle \{\chi(x) - \langle\chi\rangle\} \{\chi(x+r) - \langle\chi\rangle\} \rangle \quad (9)$$

and, obviously,

$$R(r) = R(0) - D(r)/2. \quad (10)$$

This equation implies that $\lim_{r\to\infty} D(r) = 2R(0)$.

The spectrum of $\chi(x)$ is

$$F(k) = \frac{1}{2\pi}\int_{-\infty}^{\infty} R(r)\,\mathrm{e}^{-\mathrm{i}kr}\,\mathrm{d}r = \frac{1}{\pi}\int_{0}^{\infty} R(r)\,\cos(kr)\,\mathrm{d}r$$

$$= \frac{1}{\pi}\int_{0}^{\infty}\left\{R(0) - \frac{D(r)}{2}\right\}\cos(kr)\,\mathrm{d}r. \tag{11}$$

By partial integration we get

$$F(k) = \frac{1}{2\pi k}\int_{0}^{\infty}\frac{\mathrm{d}D}{\mathrm{d}r}\,\sin(kr)\,\mathrm{d}r. \tag{12}$$

Kaimal & Finnigan (1994) have a useful discussion of structure functions and from this we conclude that for local isotropy where r is much smaller than the length scales of the flow field we have

$$D(r) = C^2\,r^{2/3}, \tag{13}$$

where C is a constant with the dimension $\dim[\chi] \times \mathrm{length}^{-1/3}$.

Inserting in (12), we get

$$F(k) = \frac{C^2}{2\pi k}\,\frac{2}{3}\int_{0}^{\infty}\frac{\sin(kr)}{r^{1/3}}\,\mathrm{d}r = \frac{C^2 k^{-5/3}}{3\,\Gamma(1/3)}. \tag{14}$$

It follows from (6) and (7) that

$$E_T(k) = \frac{10}{3}\,F_T(k) = \underbrace{\frac{10}{9\,\Gamma(1/3)}}_{\simeq 0.41}\,C_T^2\,k^{-5/3} \tag{15}$$

and

$$E_U(k) = \frac{55}{9}\,F_U(k) = \underbrace{\frac{55}{27\,\Gamma(1/3)}}_{\simeq 0.76}\,C_V^2\,k^{-5/3} \tag{16}$$

With these last two expressions the cross section (1) can be written

$$\eta(\gamma) = \underbrace{\frac{5}{9\Gamma(1/3)2^{17/3}}}_{\simeq 4.08\times 10^{-3}}\,k^{1/3}\,\frac{\cos^2(\gamma)}{\sin^{11/3}(\gamma/2)}\left\{\frac{C_T^2}{T^2} + \frac{22}{3}\,\frac{C_V^2}{c^2}\,\cos^2(\gamma/2)\right\}. \tag{17}$$

The two terms are shown in arbitrary units in Fig. 3. We note that the scattering cross section pertaining to velocity fluctuations is zero for $\gamma = \pi = 180°$. In other words, there is not backscattering from velocity fluctuations. This means that monostatic sodars are useful only when there are temperature fluctuations. In situations with neutral temperature stratification the signal quality in a monostatic sodar is pure. The scattering from temperature fluctuations is zero only for $\gamma = \pi/2 = 90°$ for which the scattering from velocity fluctuations is also zero.

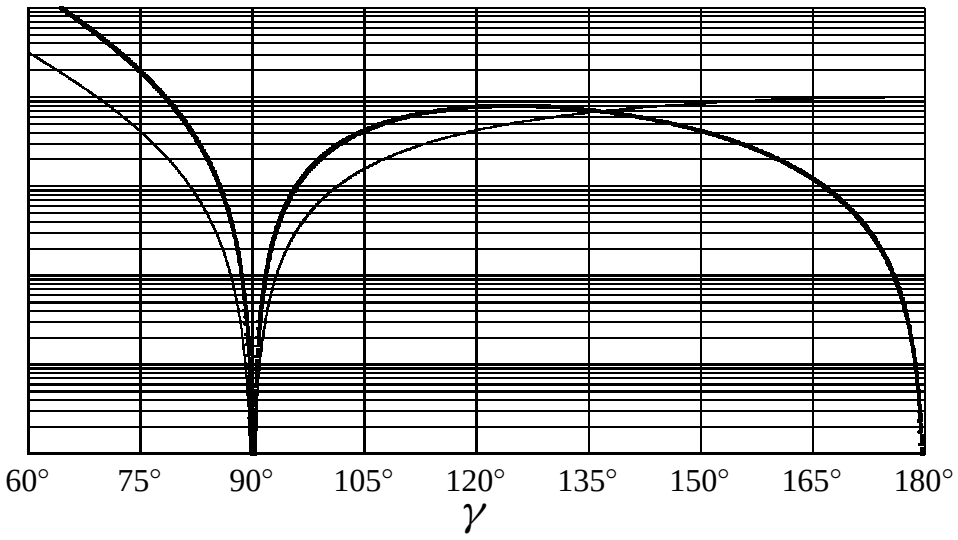

Figure 3. The scattering cross sections for velocity fluctuations (thick line) and temperature fluctuations (thin line) in arbitrary units as functions of the scattering angle γ.

It is useful to determine the relation between C_V and C_T on one side and more traditional parameters describing turbulence.

According to Panofsky & Dutton (1984) we have in the case of local isotropy

$$E_T(k) = b\,N\,\varepsilon^{-1/3}\,k^{-5/3} \tag{18}$$

and

$$E_U(k) = \alpha\,\varepsilon^{2/3}\,k^{-5/3}. \tag{19}$$

Here N and ε are the rates of destruction of specific (i.e. per unit mass) variance of temperature, ϑ, and velocity, u, in the flow direction:

$$N = 3\,\frac{\nu}{\mathrm{Pr}}\left\langle\left(\frac{\partial\vartheta}{\partial x}\right)^2\right\rangle, \tag{20}$$

$$\varepsilon = 15\,\nu\left\langle\left(\frac{\partial u}{\partial x}\right)^2\right\rangle, \tag{21}$$

where ν is the molecular diffusivity and Pr the Prandtl number. In fact, ν/Pr is, by definition, the molecular diffusivity for temperature. For the atmosphere $\nu \simeq 1.5\times10^{-5}\mathrm{m^2\,s^{-1}}$ and $\mathrm{Pr} \simeq 0.72$.

The constants b and α are dimensionless and about 1.3 (Kaimal & Finnigan 1994) and 1.7 (Frenzen & Hart 1983, Kristensen et al. 1989), respectively.

Comparing (18) and (19) to (15) and (16), we find

$$C_T^2 = \underbrace{\frac{9\,\Gamma(1/3)}{10}\,b}_{\simeq 3.13}\,N\,\varepsilon^{-1/3} \tag{22}$$

and

$$C_V^2 = \underbrace{\frac{27\,\Gamma(1/3)}{55}\,\alpha}_{\simeq 2.24}\,\varepsilon^{2/3}. \tag{23}$$

Surface-Layer Approximations

We can express ε and N in terms of measured, vertical fluxes of horizontal velocity fluctuations u' and potential temperature fluctuations ϑ'. Using standard notation (Panofsky & Dutton 1984), we first define the friction velocity

$$u_* = -\langle w'u' \rangle \tag{24}$$

and the temperature scaling parameter

$$T_* = -\frac{\langle w'\vartheta' \rangle}{u_*}, \tag{25}$$

where w' is the fluctuation vertical velocity component. The Monin-Obukhov length is then defined as

$$L = \frac{u_*^2 T}{\kappa\, g\, T_*}, \tag{26}$$

where $\kappa \simeq 0.4$ is the von Kármán constant, g the acceleration of gravity and T the air temperature. The stratification of the atmosphere can then be characterized by the height z and L in the form

$$\frac{z}{L} = \kappa z\,\frac{g}{T}\,\frac{T_*}{u_*^2}. \tag{27}$$

For local, turbulent balance between production and destruction we have (Panofsky & Dutton 1984)

$$\varepsilon = \frac{u_*^3}{\kappa z}\,\varphi_m\Big(\frac{z}{L}\Big) - \frac{g}{T}\,u_* T_* = \frac{u_*^3}{\kappa z}\underbrace{\Big\{\varphi_m\Big(\frac{z}{L}\Big) - \frac{z}{L}\Big\}}_{\varphi_\varepsilon\left(\frac{z}{L}\right)} \tag{28}$$

and

$$N = \frac{u_* T_*^2}{\kappa z}\,\varphi_h\Big(\frac{z}{L}\Big), \tag{29}$$

where φ_m, φ_ε, and φ_h are the supposedly well-known, diabatic functions for the atmospheric surface layer.

We now get

$$C_V^2 = \frac{27\,\Gamma(1/3)}{55}\,\alpha\,\frac{u_*^2}{(\kappa z)^{2/3}}\,\varphi_\varepsilon^{2/3}\Big(\frac{z}{L}\Big) \tag{30}$$

and

$$\frac{C_T^2}{C_V^2} = \frac{11}{6}\,\frac{b}{\alpha}\,\frac{N}{\varepsilon} = \frac{11}{6}\,\frac{b}{\alpha}\,\frac{T_*^2}{u_*^2}\,\underbrace{\frac{\varphi_h\Big(\frac{z}{L}\Big)}{\varphi_\varepsilon\Big(\frac{z}{L}\Big)}}_{\varphi_{T/V}\left(\frac{z}{L}\right)}. \tag{31}$$

Following Carl et al. (1973) and Panofsky & Dutton (1984), the basic standard diabatic functions for an unstable surface layer are

$$\varphi_m(\zeta) = (1 + 15|\zeta|)^{-1/3} \tag{32}$$

and

$$\varphi_h(\zeta) = \varphi_m^2(\zeta). \tag{33}$$

The two functions $\varphi_\varepsilon(z/L)$ and $\varphi_{T/V}(z/L)$ are displayed in Fig. 4 for the unstable surface layer.

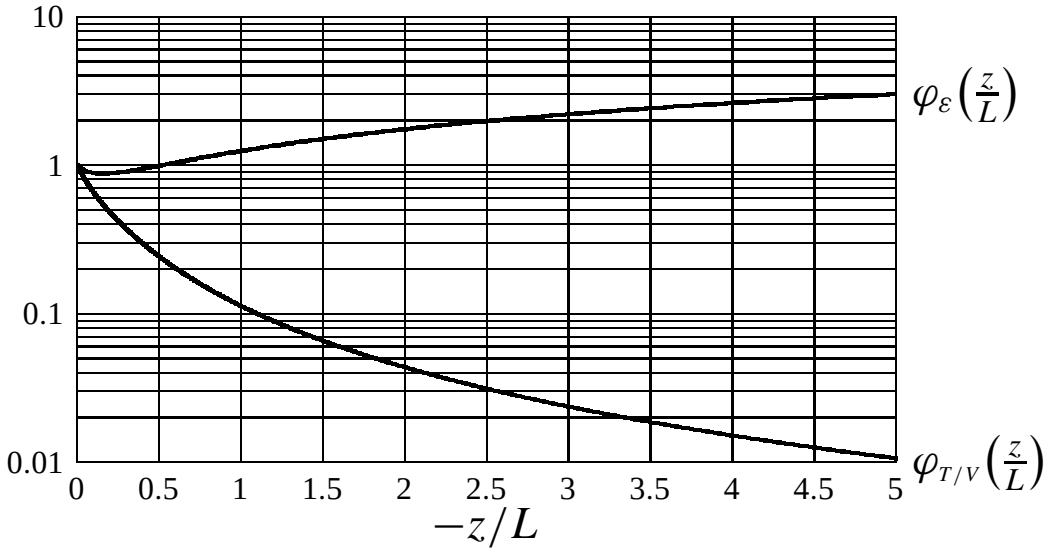

Figure 4. The functions $\varphi_\varepsilon(z/L)$ and $\varphi_{T/V}(z/L)$ for the unstable surface layer.

We see that C_V^2 and C_T^2 depend on z, u_*, and the sensible heat flux

$$H = \rho\, c_p\, \langle w'\vartheta' \rangle. \tag{34}$$

Here $\rho = 1.293\,\mathrm{kg/m^3}$ and $c_p = 1005.7\,\mathrm{J/m^3/K}$ are the density and the specific heat capacity for constant pressure of dry air. Figures 5 and 6 show C_V^2 and C_T^2 as functions of u_* and H at the altitude $z = 60$ m. With the surface modeling outlined above, C_T^2 becomes infinity when the friction velocity u_* vanishes and therefore the lowest value here is $u_* = 0.01\,\mathrm{m/s}$.

We rewrite (17) in terms of these new definitions

$$\eta(\gamma) = \eta_V(\gamma) + \eta_T(\gamma), \tag{35}$$

where

$$\eta_V(\gamma) = \underbrace{\frac{\alpha}{\Gamma(1/3)\,2^{14/3}}}_{\simeq 0.025}\, k^{1/3} \left(\frac{\varphi_\varepsilon}{\kappa\, z}\right)^{2/3} \frac{u_*^2}{c^2}\, \frac{\cos^2(\gamma)\cos^2(\gamma/2)}{\sin^{11/3}(\gamma/2)} \tag{36}$$

and

$$\eta_T(\gamma) = \underbrace{\frac{b}{\Gamma(1/3)\,2^{14/3}}}_{\simeq 0.0048}\, k^{1/3} \left(\frac{\varphi_\varepsilon}{\kappa\, z}\right)^{2/3} \varphi_{T/V}\left(\frac{z}{L}\right) \frac{T_*^2}{T^2}\, \frac{\cos^2(\gamma)}{\sin^{11/3}(\gamma/2)}. \tag{37}$$

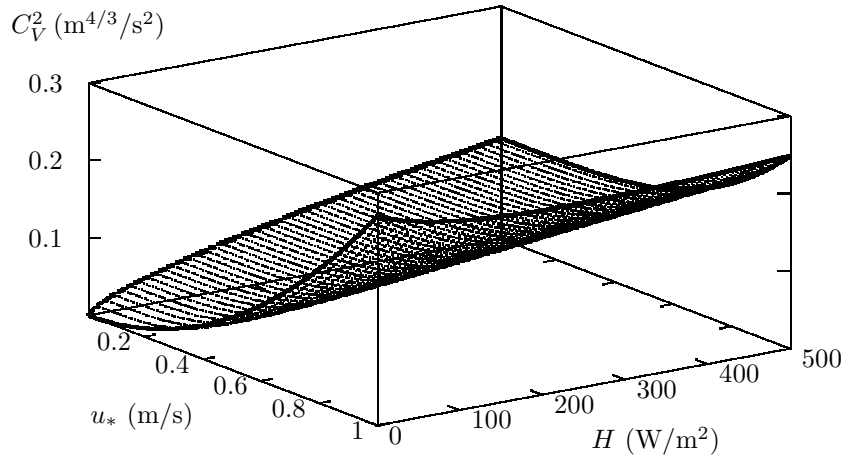

Figure 5. C_V^2 *at* $z = 60\,\mathrm{m}$ *for* $0.01\,\mathrm{m/s} \leq u_* \leq 1\,\mathrm{m/s}$ *and* $0\,\mathrm{W/m^2} \leq H \leq 500\,\mathrm{W/m^2}$.

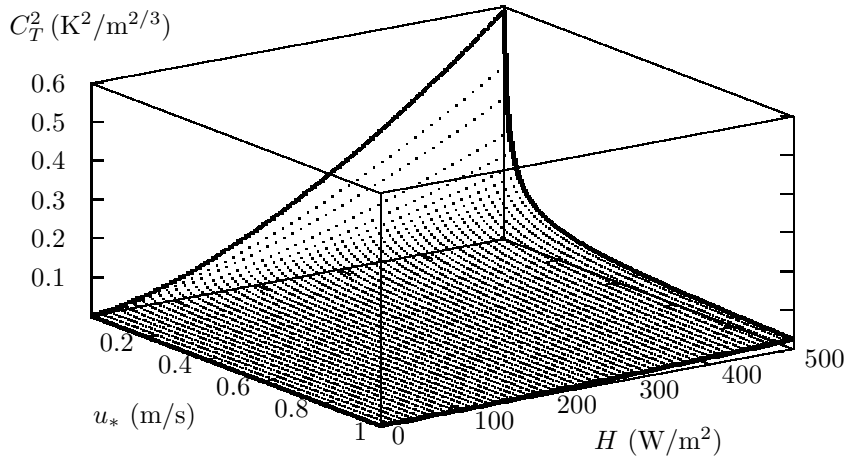

Figure 6. C_T^2 *at* $z = 60\,\mathrm{m}$ *for* $0.01\,\mathrm{m/s} \leq u_* \leq 1\,\mathrm{m/s}$ *and* $0\,\mathrm{W/m^2} \leq H \leq 500\,\mathrm{W/m^2}$.

These last two equations, together with Fig. 3 illustrates the difference between monostatic and bistatic sodar operation. In the first case $\gamma = 180°$ which means that $\eta_V = 0$, i.e. that the velocity eddies do not scatter sound in the direction of the emitter. For a bistatic sodar with $\gamma \simeq 135°$ both temperature and velocity fluctuations have about their maximum contribution to the total scattering cross section. This will, all considered, give nearly the strongest possible return signal. Figure 7 shows the cross-section ratio η_T/η_V for the scattering angle $\gamma = 135°$ at the height $z = 60$ m as a function of the friction velocity u_* in the interval from 0.2 m/s to 1 m/s and the sensible heat flux H from 0 to 500 W m^{-2}. We note that only when the friction velocity is small and the heat flux large will η_T be larger than η_V for this geometry. We see that there are two advantages in using a bistatic sodar:

1. the instrument can operate with a strong return signal even when the atmosphere is neutrally stratified ($T_* = 0 \Rightarrow \eta_T = 0$), because in general $\eta_V > 0$ in this situation, and
2. it can be operated in a continuous mode, because the transmitter and the

receiver are separated.

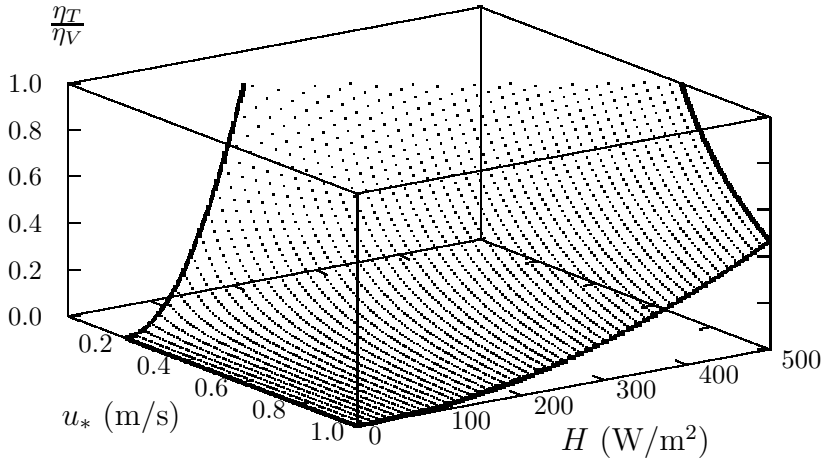

Figure 7. The cross-section ratio η_T/η_V for the scattering angle $\gamma = 135°$ at the height $z = 60$ m as a function of the friction velocity u_* and the sensible heat flux H.

2.2 The Bistatic Sodar Equation

Here we follow the approach by Kristensen et al. (1978), Kristensen (1978), and Neff & Coulter (1986) to derive the *sodar equation* which tells how much acoustic energy is received by a microphone at a certain distance from a loud speaker.

A bistatic sodar consists of a transmitter T, which is a powerful loudspeaker, and a sound receiver R. They are located a certain distance $2d$ from one another. The monochromatic sound from T has a wavelength of about 0.5 m or less and this means that just a few meters from T or R we are in the far-field zone where the sound pressure is inversely proportional to the square of the distance r from T or R (if the last is used as a speaker). However, the transmission and reception are not isotropic. Each are characterized by the an angle ψ from the axis of T or R. If we let the emitted power be P_T then the power flux, per unit solid angle, from T at the distance r will be

$$\mathcal{F}_\mathsf{T}(r,\psi) = \frac{P_\mathsf{T}}{r^2} F_\mathsf{T}(\psi)\, \mathrm{e}^{-\beta r}, \tag{38}$$

where $F_\mathsf{T}(\psi)$ is the so-called directivity of the transmitter, defined so that the integral over the whole hemisphere is one, i.e.

$$2\pi \int_0^\pi F_\mathsf{T}(\psi) \sin\psi \, \mathrm{d}\psi = 1, \tag{39}$$

and $\beta \sim 10^{-3}\,\mathrm{m}^{-1}$ the attenuation coefficient. The directivity of the receiver $F_\mathsf{R}(\psi)$ is defined in the same way. Further, it is necessary to characterize R by an receiving area A since the received power is proportional to this area.

The received power is a function of the total distance the sound has traveled from T to R. Calling this distance $2a$ (for reasons which will be clear below), the attenuation is $\exp(-2a\beta)$.

The transmitter and the receiver are installed in such a way that they intersect in a vertical plane and their angles with the horizontal baseline between them are denoted ϕ_0 and ϕ_0', respectively.

Since we want to include the attenuation in the calculation of the power received by R we look for the foci of points where the travel distance from T to R is the same, namely $2a$. These foci are an axisymmetric ellipsoid with the major half axis a and the two half minor axes $\sqrt{a^2 - d^2}$. The geometry is shown in Fig. 8 in a Cartesian coordinate system where also the symbols is explained.

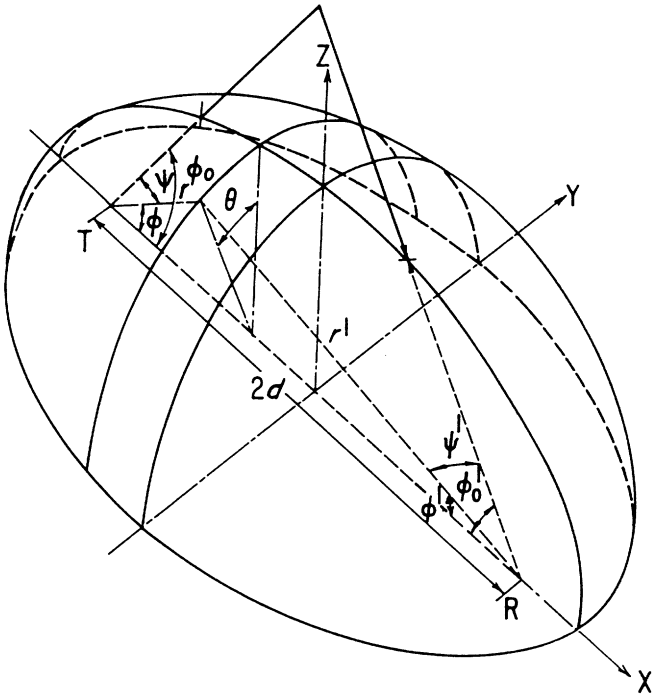

Figure 8. Sodar Geometry. The transmitter T *and the receiver* R *are located at the points* $(-d/2, 0, 0)$ *and* $(d/2, 0, 0)$ *in an* XYZ *coordinate system. The axes of* T *and* R *intersect in a vertical plane. The angles between* T *and* R *and the baseline between them are* ϕ_0 *and* ϕ_0'*. The axisymmetric ellipsoid with half major axis* a *and half minor axes* $\sqrt{a^2 - d^2}$ *is shown and the distances* r *and* r' *from a point* (x, y, z) *on the ellipsoid to* T *and* R *are indicated as well as the angle* θ *between the vertical plane and the plane through this point and the* X*-axis. Also shown are the angles* ϕ *and* ϕ' *between the* X*-axis and the lines from* T *and* R *to the point* (x, y, z)*, together with the angles* ψ *and* ψ' *from the axes of* T *and* R*. From Neff & Coulter (1986).*

In polar coordinates the ellipsoid can be described in polar coordinates with the pole in T by the equation

$$r = \frac{a^2 - d^2}{a - d\cos\phi}. \tag{40}$$

Inspecting Fig. 8, we see that the scattering angle γ entering (17) can be expressed in terms of ϕ and ϕ' by

$$\gamma = \phi + \phi'. \tag{41}$$

Plane geometrical analysis of the triangle defined by the points $(-d/2, 0, 0)$, $(d/2, 0, 0)$, and (x, y, z) yields the following relations between ϕ and ϕ'

$$\cos\phi' = \frac{2ad - (a^2 + d^2)\cos\phi}{d^2 \sin^2\phi + (a - d\cos\phi)^2}, \tag{42}$$

which implies

$$\sin\phi' = \frac{(a^2 - d^2)\sin\phi}{d^2 \sin^2\phi + (a - d\cos\phi)^2}. \tag{43}$$

We can consequently express the scattering angle γ in terms of ϕ by

$$\cos\gamma = \cos\phi\cos\phi' - \sin\phi\sin\phi' = \frac{d^2\sin^2\phi - (a - d\cos\phi)^2}{d^2\sin^2\phi + (a - d\cos\phi)^2} \tag{44}$$

or by the useful alternatives

$$\cos(\gamma/2) = \frac{d\sin\phi}{\sqrt{d^2\sin^2\phi + (a - d\cos\phi)^2}} \tag{45}$$

and

$$\sin(\gamma/2) = \frac{a - d\cos\phi}{\sqrt{d^2\sin^2\phi + (a - d\cos\phi)^2}}. \tag{46}$$

According to the definition of the ellipsoid the sum of r and r' is equal to $2a$ and this means that r' can also be expressed in terms of a and ϕ. We have

$$r' = 2a - r = \frac{d^2\sin^2\phi + (a - d\cos\phi)^2}{a - d\cos\phi}. \tag{47}$$

Applying the cosine relation for spherical triangles we get

$$\begin{aligned} \cos\psi &= \cos\phi_0\cos\phi + \sin\phi_0\sin\phi\cos\theta \\ &= \cos(\phi - \phi_0) - \sin\phi_0\sin\phi\,(1 - \cos\theta) \end{aligned} \tag{48}$$

and

$$\begin{aligned} \cos\psi' &= \cos\phi_0'\cos\phi' + \sin\phi_0'\sin\phi'\cos\theta \\ &= \cos(\phi' - \phi_0') - \sin\phi_0'\sin\phi'\,(1 - \cos\theta). \end{aligned} \tag{49}$$

In small-angle approximation which is relevant here, we may reformulate (48) and (49) in the following way:

$$\psi^2 = (\phi - \phi_0)^2 + \theta^2\sin^2\phi_0 \tag{50}$$

and

$$\psi'^2 = (\phi' - \phi_0')^2 + \theta^2\sin^2\phi_0'. \tag{51}$$

Since we want to determine the power received by R from each points, we need to calculate the volume δV corresponding to increments $(\delta x, \delta y, \delta z)$ around the point (x, y, z). Translating to increments $(\delta a, \delta\phi, \delta\theta)$ around the same point defined by (a, ϕ, θ), we write

$$\delta V = \delta x\, \delta y\, \delta z = \frac{\partial(x, y, z)}{\partial(a, \phi, \theta)}\, \delta a\, \delta\phi\, \delta\theta, \tag{52}$$

where

$$\frac{\partial(x, y, z)}{\partial(a, \phi, \theta)} = \left\| \begin{array}{ccc} \frac{\partial x}{\partial a} & \frac{\partial y}{\partial a} & \frac{\partial z}{\partial a} \\ \frac{\partial x}{\partial \phi} & \frac{\partial y}{\partial \phi} & \frac{\partial z}{\partial \phi} \\ \frac{\partial x}{\partial \theta} & \frac{\partial y}{\partial \theta} & \frac{\partial z}{\partial \theta} \end{array} \right\|, \tag{53}$$

is the Jacobian, and where

$$\left\{ \begin{array}{c} x \\ y \\ z \end{array} \right\} = \left\{ \begin{array}{l} r\, \cos\phi - d \\ r\, \sin\phi\, \sin\theta \\ r\, \sin\phi\, \cos\theta \end{array} \right\} \tag{54}$$

with the constraint (40). The Jacobian becomes

$$\frac{\partial(x, y, z)}{\partial(a, \phi, \theta)} = r^2\, \frac{\partial r}{\partial a}\, \sin\phi = \frac{(a^2 - d^2)^2 \left\{ d^2 \sin^2\phi + (a - d\cos\phi)^2 \right\}}{(a - d\cos\phi)^4}\, \sin\phi. \tag{55}$$

The power flux at the point (x, y, z), given by (54), is $\mathcal{F}_{\mathsf{T}}(r, \psi)$ as stated in (38). From a small volume δV around this point the power scattered per steradian in the direction towards R is thus

$$\delta P_{\mathrm{s}} = \mathcal{F}_{\mathsf{T}}(r, \psi) \times \delta V \times \eta(\gamma) = P_{\mathsf{T}}\, \frac{F_{\mathsf{T}}(\psi)}{r^2}\, \mathrm{e}^{-\beta r}\, \eta(\gamma)\, \delta V. \tag{56}$$

The power δP_{R} received by R is proportional to the solid angle A/r'^2 subtended by R as seen from the point (x, y, z):

$$\delta P_{\mathsf{R}} = \delta P_{\mathrm{s}} \times \frac{A}{r'^2}\, F_{\mathsf{R}}(\psi')\, \mathrm{e}^{-\beta r'}, \tag{57}$$

where the directivity of the receiver is also taken into account.

Finally we get

$$\frac{\delta P_{\mathsf{R}}}{\delta a\, \delta\phi\, \delta\theta} = P_{\mathsf{T}} \frac{A\, F_{\mathsf{T}}(\psi)\, F_{\mathsf{R}}(\psi')\, \eta(\gamma)}{d^2 \sin^2\phi + (a - d\cos\phi)^2}\, \sin\phi\, \mathrm{e}^{-2\beta\, a}, \tag{58}$$

which, in view of (42)–(46), (48), and (49), is a function of only a, ϕ, and θ.

In this form the sodar equation was used by Kristensen et al. (1978), Kristensen (1978), and Neff & Coulter (1986) to determine the received power by R as a function of time when a short pulse was emitted from T. This is obtained by integrating over θ and ϕ and interpreting a as a measure of time, which is possible because the time t elapsed after the time of emission of the sound pulse t_0 is $t = 2a/c + t_0$.

Sound Attenuation

The atmospheric sound attenuation parameter β is a rather complicated function of frequency f (Hz), temperature T (C°), relative humidity RH (%), and atmospheric pressure p (hPa). This function is given by the International Standard ISO 9613-1:1993(E) according to Salomons (2001) who provides a practical, engineering equation for β. Unless the atmospheric conditions are extreme, the accuracy is $\pm 10\,\%$.

A function which depends on four variables in a complicated manner is difficult to illustrate graphically in a quantitative as well as qualitative manner. Fortunately, the dependence on the atmospheric pressure is week, less than 0.1 % in the range $950 < p < 1050\,\mathrm{hPa}$ when $T = 20°$, RH=50%, and f=1000 Hz.

In Figs. 9, 10, and 11 the attenuation parameter is shown graphically as functions of frequency, temperature and relative humidity with the other three parameters kept fixed.

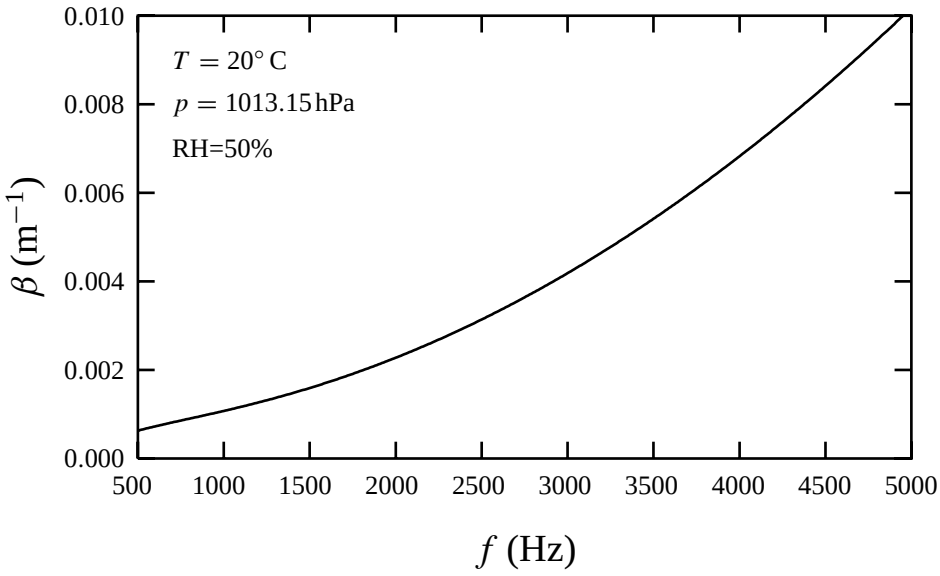

Figure 9. Example of attenuation parameter as a function of frequency.

Obviously the attenuation parameter is very sensitive to frequency, varying a factor of 10 when the frequency varies from 1000 Hz to 5000 Hz. However, the dependencies on temperature and relative humidity are also very pronounced and non-monotone.

In order to illustrate the variation of the attenuation as function of temperature and humidity simultaneously Fig. 12 gives an impression of how complicated the function $\beta(f, T, RH, p)$ is. The two surfaces correspond to two different frequencies at $p = 1013.25\,\mathrm{hPa}$.

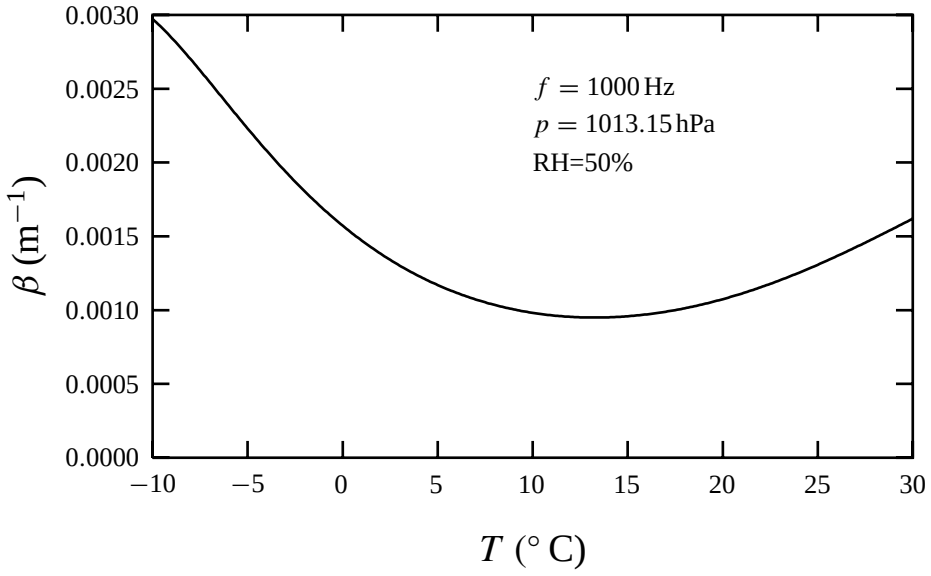

Figure 10. Example of attenuation parameter as a function of temperature.

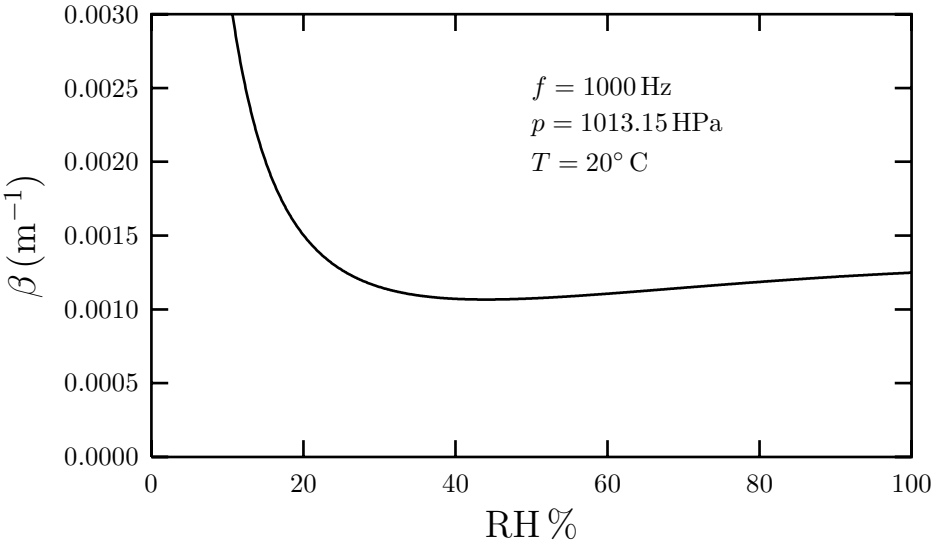

Figure 11. Example of attenuation parameter as a function of relative humidity.

Antenna Directivity

The directivities $F_{\mathsf{T}}(\psi)$ and $F_{\mathsf{R}}(\psi')$ must be experimentally determined, but we assume here they both have the form

$$F(\psi) = \frac{\exp\left(-\dfrac{\psi^2}{2\sigma^2}\right)}{2\pi\sigma^2}, \tag{59}$$

which fulfill the normalization (39). The antenna area is related to the angular width σ^2. To see this, let us consider a circular transmitter with the area $A = \pi \times R^2$. Figure 13 illustrates the situation.

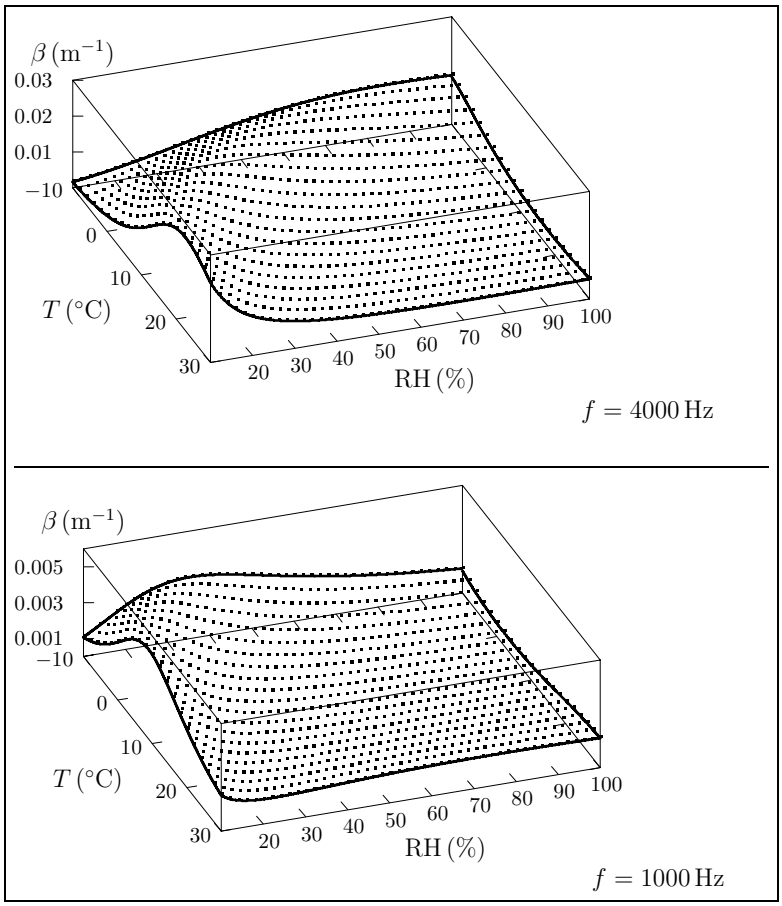

Figure 12. The attenuation coefficient as function of temperature and relative humidity for $f = 4000\,Hz$ (top frame) and for $f = 1000\,Hz$ (bottom frame).

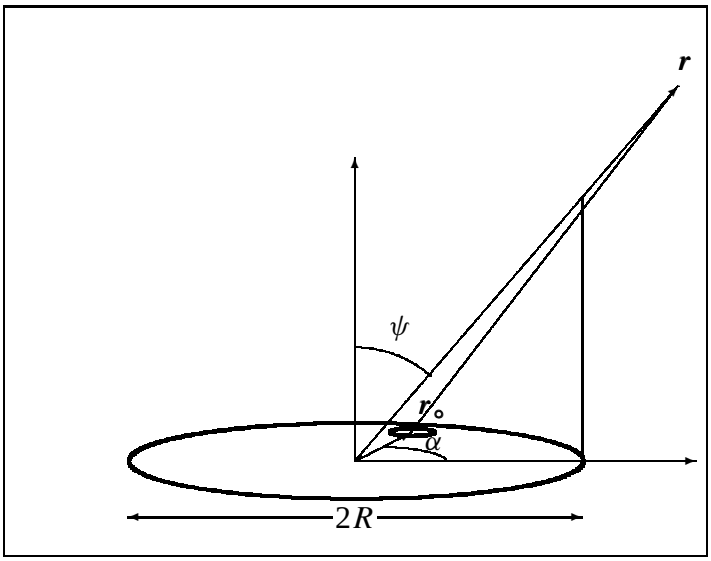

Figure 13. The circular antenna disk with radius R transmits sound with wave number k with uniform density from the entire disk to a point at r. This vector forms the angle ψ with the antenna axis. The contribution from a small antenna area, characterized by the distance $r_\circ$ from the axis and the azimuth α, is indicated.

The sound pressure arriving at r is proportional to

$$I(r,\psi) = \int_0^R r_\circ \,\mathrm{d}r_\circ \int_0^{2\pi} \mathrm{d}\alpha \,\frac{\mathrm{e}^{\mathrm{i}k|r-r_\circ|}}{|r-r_\circ|}. \tag{60}$$

In the far-field approximation, where $r \gg R$, we have

$$|r-r_\circ| = \sqrt{r^2 - 2rr_\circ \sin\psi\cos\alpha + r_\circ^2} \approx r - r_\circ \sin\psi\cos\alpha, \tag{61}$$

so that

$$\begin{aligned} I(r,\psi) &= \int_0^R r_\circ \,\mathrm{d}r_\circ \int_0^{2\pi} \mathrm{d}\,\alpha \,\frac{\mathrm{e}^{\mathrm{i}kr - \mathrm{i}kr_\circ \sin\psi\cos\alpha}}{r} \\ &= \frac{\mathrm{e}^{\mathrm{i}kr}}{r} \int_0^R r_\circ \,\mathrm{d}r_\circ \int_0^{2\pi} \mathrm{d}\,\alpha \,\mathrm{e}^{-\mathrm{i}kr_\circ \sin\psi\cos\alpha} \\ &= 2\pi \,\frac{\mathrm{e}^{\mathrm{i}kr}}{r} \int_0^R \mathrm{J}_0(kr_\circ \sin\psi)\, r_\circ \,\mathrm{d}r_\circ = 2\pi\, R^2 \,\frac{\mathrm{e}^{\mathrm{i}kr}}{r}\,\frac{\mathrm{J}_1(kR\sin\psi)}{kR\sin\psi}, \end{aligned} \tag{62}$$

where $\mathrm{J}_n(x)$ is the Bessel function of the first kind, of order n. The dimensionless quantity Rk is usually much larger than one so that $\sin\psi$ can be replaced by ψ. The directivity is proportional to $|I(r,\psi)|^2$. We demand that this directivity and its derivative with respect to ψ has the same value as (59) for $\psi = 0$. This means that

$$\left(\frac{2\mathrm{J}_1(kR\psi)}{kR\psi}\right)^2 \simeq \exp\left(-\frac{\psi^2}{2\sigma^2}\right) \tag{63}$$

with

$$2 = \sigma^2\, k^2 R^2. \tag{64}$$

The implications is that

$$k^2 \times A = \frac{2\pi}{\sigma^2}. \tag{65}$$

The difference between left-hand side and right-hand sidelobe of (63) is illustrated by Fig. 14.

Continuous-Wave Operation

I this section we use the result (58) to evaluate the *scattering strength*, i.e. the spatial distribution of scattered power flux, received by R when T is operated continuously.

To obtain a spatial distribution of the scattering strength we first transform (58) into Cartesian coordinates:

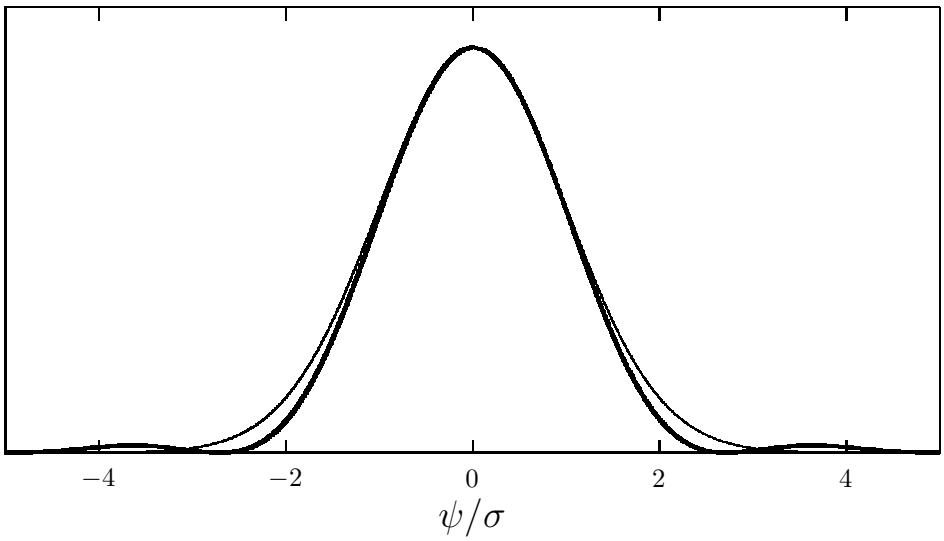

Figure 14. The antenna directivity $F(\psi)$. Thick line: left-hand side of (63), thin line: right-hand side of (63).

$$W(x,y,z) = \frac{\delta P_{\mathsf{R}}}{\delta x\,\delta y\,\delta z} = \frac{\delta P_{\mathsf{R}}}{\delta a\,\delta\phi\,\delta\theta}\left(\frac{\partial(x,y,z)}{\partial(a,\phi,\theta)}\right)^{-1}$$
$$= P_{\mathsf{T}}\,A\,F_{\mathsf{T}}(\psi)\,F_{\mathsf{R}}(\psi')\,\eta(\gamma)\frac{(a-d\,\cos\phi)^4 \mathrm{e}^{-2\beta a}}{(a^2-d^2)^2\left\{d^2\sin^2\phi+(a-d\,\cos\phi)^2\right\}^2}. \quad (66)$$

For a given Cartesian set of coordinates (x,y,z) we obtain the corresponding polar coordinates r, ϕ, and θ with origin at the transmitter by solving (54):

$$r = \left\{(x+d)^2+y^2+z^2\right\}^{1/2}, \quad (67)$$

$$\phi = \mathrm{arctan2}\Big(x+d, \sqrt{y^2+z^2}\Big), \quad (68)$$

$$\theta = \mathrm{arctan2}(z,y), \quad (69)$$

where

$$\mathrm{arctan2}(x,y) = \begin{cases} \pi, & y=0\,\&\,x\le 0 \\ 2\,\arctan\left(\dfrac{y}{\sqrt{x^2+y^2}+x}\right), & \text{elsewhere} \end{cases}. \quad (70)$$

Solving (40) for a, we get

$$a = \frac{r}{2} + \left\{\left(\frac{r}{2}-d\cos\phi\right)^2 + d^2\sin^2\phi\right\}. \quad (71)$$

The scattering angle γ is obtained from (45) and (46):

$$\gamma = 2\,\mathrm{arctan2}(d\sin\phi, a-d\cos\phi). \quad (72)$$

In order to calculate the directivities $F_{\mathsf{T}}(\psi)$ and $F_{\mathsf{R}}(\psi')$ we must first determine ϕ' by the equation

$$\phi' = \arctan2\left(2ad - (a^2+d^2)\cos\phi, (a^2-d^2)\sin\phi\right), \tag{73}$$

which is a consequence of (42) and (43).

Figure 15 illustrates the scattering-strength distribution around the point (x_0, y_0, z_0) where the transmitter and receiver axes intersect in the case $\phi_0 = 90°$. Since we specify the length $2d$ of the baseline and the inclinations ϕ_0 and ϕ_0', this point becomes

$$\left\{ \begin{array}{c} x_0 \\ y_0 \\ z_0 \end{array} \right\} = \frac{1}{a_0 - d\cos\phi_0} \left\{ \begin{array}{c} a_0(a_0\cos\phi_0 - d) \\ 0 \\ (a_0^2 - d^2)\sin\phi_0 \end{array} \right\}, \tag{74}$$

where

$$a_0 = d\,\frac{\sin\phi_0 + \sin\phi_0'}{\sin(\phi_0 + \phi_0')}. \tag{75}$$

In these considerations the dependence of the scattering cross section on the height z has not been taken into consideration. However, inspecting (36) and (37) we see that there is a dependence on height z. In principle this height dependence can be taken correctly into account when we know the surface heat flux, i.e. the temperature stratification. If we leave the general case and consider only neutral stratification the situation is somewhat simpler. Applying (36) to (66), we get

$$\begin{aligned} &\frac{W(x,y,z)\,d^3}{P_{\mathsf{T}}\,(A/d^2)\,(u_*^2/c^2)\,(kd)^{1/3}} = \\ &\quad \underbrace{\frac{\alpha\,\kappa^{-2/3}}{2^{14/3}}}_{\simeq 0.124} \frac{\cos^2(\gamma)\,\cos^2(\gamma/2)}{\sin^{11/3}(\gamma/2)} F_{\mathsf{T}}(\psi) F_{\mathsf{R}}(\psi')\,\exp(-2\beta d\,(a/d)) \\ &\quad \times \frac{\left\{(a/d)^2 - \cos\phi\right\}^4}{(z/d)^{2/3}\,\left\{(a/d)^2 - 1\right\}^2\,\left\{\sin^2\phi + (a/d - \cos\phi)^2\right\}^2}. \end{aligned} \tag{76}$$

We may calculate the received power by integrating (58) over $d \le a < \infty$, $0 \le \phi < \pi$ and $\pi/2 \le \theta < \pi/2$. Introducing the dimensionless variable

$$\xi = \frac{a}{d}, \tag{77}$$

we have

$$\begin{aligned} \frac{\delta P_{\mathsf{R}}}{P_{\mathsf{T}}\delta\xi\,\delta\phi\,\delta\theta} &= \underbrace{\frac{\alpha\,\kappa^{-2/3}}{2^{20/3}\,\pi}}_{\simeq 0.01} \frac{u_*^2}{c^2}\,\frac{A}{d^2}\,(kd)^{1/3} \\ &\quad \times \frac{\cos^2(\gamma)\,\cos^2(\gamma/2)}{\sin^{11/3}(\gamma/2)}\,\mathrm{e}^{-2\beta d\xi}\,\exp\left(-\frac{(\phi-\phi_0)^2}{2\sigma_{\mathsf{T}}^2} - \frac{(\phi'-\phi_0')^2}{2\sigma_{\mathsf{R}}^2}\right) \\ &\quad \times \left(\frac{\xi - \cos\phi}{\xi^2 - 1}\right)^{2/3} \frac{\sin^{1/3}\phi}{\sin^2\phi + (\xi - \cos\phi)^2} \\ &\quad \times \cos^{-2/3}\theta\,\exp\left(-\left\{\frac{\sin^2\phi_0}{2\sigma_{\mathsf{T}}^2} + \frac{\sin^2\phi_0'}{2\sigma_{\mathsf{R}}^2}\right\}\theta^2\right). \end{aligned} \tag{78}$$

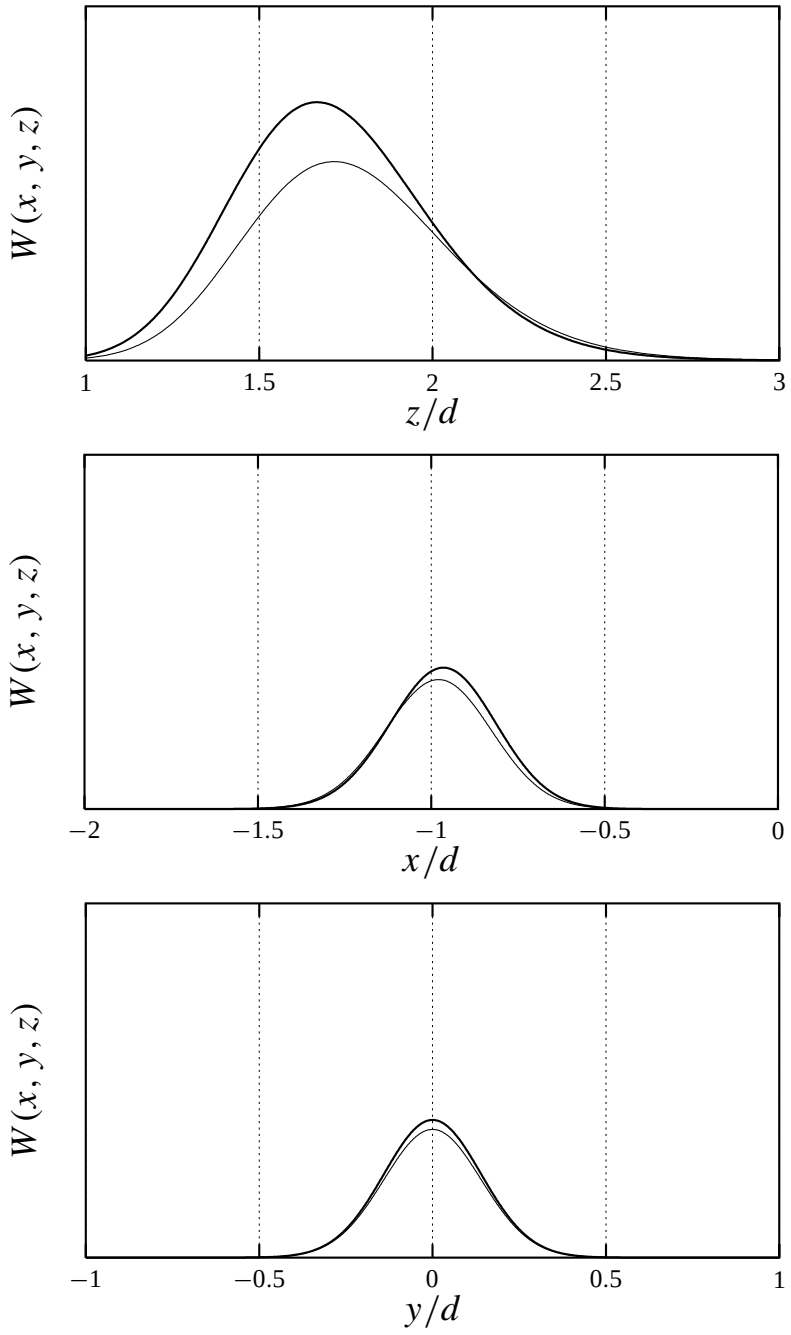

Figure 15. Line projections of the scattering-strength distribution through the intersection of the axes of T *and* R *for* $\beta d = 0.5$, $\phi_0 = 90°$, $\phi_0' = 45°$, *and* $\sigma_{\mathsf{T}} = \sigma_{\mathsf{R}} = 5°$. *Top frame: vertical axis. Middle frame: horizontal axis parallel with the baseline. Bottom frame: horizontal axis perpendicular to the baseline. The scale is the same in all the frames. The thick lines (the upper curves) correspond to scattering on velocity fluctuations per unit* C_V^2/c^2 *and the thin lines (the lower curves) to temperature fluctuations per unit* C_T^2/T^2.

For $\phi_0 = 90°$, $\phi_0' = 45°$, $\sigma_\mathsf{T} = \sigma_\mathsf{R} = 2.16°$, $\beta = 0.004$ m^{-1}, and half the baseline $d = 30$ m the result is

$$\frac{P_\mathsf{R}}{P_\mathsf{T}} = \underbrace{\frac{\alpha\,\kappa^{-2/3}}{2^{14/3}}}_{\simeq 0.124} \frac{u_*^2}{c^2} \frac{A}{d^2} (kd)^{1/3} \times 0.141. \tag{79}$$

These parameters are those used in the preliminary results described in the following section for the Heimdall configuration.

Considering (78) the spatial weighting function, we may determine its center of mass $(\langle x\rangle, \langle y\rangle, \langle z\rangle)$ and rms widths $(\sigma_x, \sigma_y, \sigma_z)$. We get

$$\left\{ \begin{array}{c} \langle x\rangle \\ \langle y\rangle \\ \langle z\rangle \end{array} \right\} = \left\{ \begin{array}{r} -29.9 \\ 0.0 \\ 59.5 \end{array} \right\} \text{m} \tag{80}$$

and

$$\left\{ \begin{array}{c} \sigma_x \\ \sigma_y \\ \sigma_z \end{array} \right\} = \left\{ \begin{array}{c} 2.2 \\ 1.8 \\ 5.0 \end{array} \right\} \text{m}. \tag{81}$$

This concludes the theoretical background for bistatic sodar operation.

3 Heimdall, Description and Preliminary Results

The Heimdall bistatic sodar has been built from basic components, including hardware and software. Without going into too many details, we wish to give an impression of the function of different parts of the instrument. It has not been applied to field experiments, but rather been tested against the theory described in the preceding section.

3.1 Instrument Description

The basic design of the instrument is a sound transmitter and a sound receiver. They both have an antenna disk with identical geometry to direct and receive the sound from a rather confined spatial domain. The disks are designed to satellite reception and are almost circular, with the largest diameter equal to 1.2 m and the smallest a little less than 1 m. In the foci of these antenna disks there are a speaker and a microphone, respectively. The transmitter is shown in Fig. 16.

The directivity of each antenna have a pronounced central main lobe and the nearest sidelobe at about 10° from the axis is reduced by a factor 0.0025 (26 dB) compared to the main lobe as shown in Fig. 17. We have not determined the directivity for our antenna disks but relied on measurements carried out on a similar disk by Handwerker (1999).

The speaker is a 30 W electric-power Paso TR30-TW horn. The total power of sound is 1.58 W for 30 W electric-power input in the frequency range 1–2 kHz.

Figure 16. The Heimdall sodar transmitter at Risø. The speaker is located in the focus of the antenna disk.

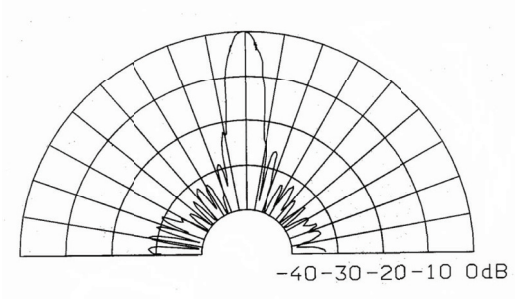

Figure 17. Polar plot of the directivity of both antennae (Handwerker 1999).

This corresponds to about $P_{\mathsf{T}} = 100\ \mathrm{W\,sr^{-1}}$, i.e. the sound power per unit solid angle, in the direction of the axis ($\pm 15°$). The horn is operated with a sine-signal input in the range 2–4 kHz.

The geometry of the receiver antenna R is identical to the transmitter T except that the horn is replaced by a condenser microphone, Brüel&Kjær type 41451, including a 4669-c preamplifier with an adjustable gain at 9, 10, 20…60 dB, and a Brüel&Kjær type 5935-1 power supply.

We tested the system against the sodar equation (7) integrated over ξ, θ, and ϕ in a configuration where $\phi_\circ = \pi/2$ and $\phi'_\circ = \pi/4$. The basic line between T and R was 60 m. Instead of (30) and (31) for C_V^2 and C_T^2, we used the investigation by Wilson & Ostashev (1998) where a surface heat flux of 250 W $\mathrm{m^{-1}}$ is taken into account in a slightly different way.

To obtain Doppler velocities the output signal is processed by a National Instruments NI 4552 Dynamic Signal Analyzer. It can handle four analogue input signals with a sample rate which can be varied in steps of $1.907 \times 10^{-4}\ \mathrm{S\,s^{-1}}$ (samples per

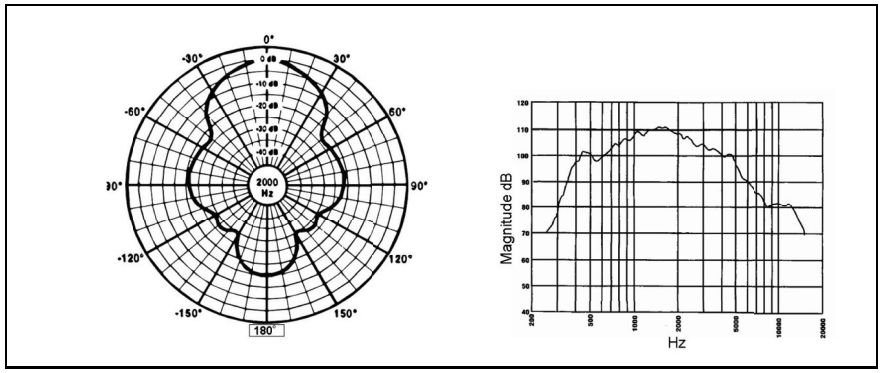

Figure 18. Polar plot of the directivity in dB radial units of the Paso TR30-TW horn at the frequency 2 kHz(left) and the efficiency as a function of the frequency with a 30 W electric input (right).

Table 1. Acoustic power flux, assuming the roughness length $z_\circ = 0.01$ m, the friction velocity $u_* = 0.2\,m\,s^{-1}$ and sensible heat flux equal to 250 $W\,m^{-2}$. The baseline is 60 m, corresponding to the same nominal height for the beam intersection. The sound attenuation parameter $\beta = 0.002$ m^{-1}. The electric power to the horn is 30 W and the transmitter frequency 4 kHz.

	$\mathrm{W\,m^{-2}}$
Contribution from temperature fluctuations	5.34×10^{-10}
Contribution from velocity fluctuations	2.64×10^{-9}
Measured	1.89×10^{-10}

second) from 5.8 to 2.048×10^5 $\mathrm{S\,s^{-1}}$. Subsequently, the digitized signal is transformed into a Doppler spectrum with a 32-bit FFT (Fast Fourier Transform). To suppress transients the analyzer makes it possible to subject the signal to various forms of windowing e.g., hanning. The effect of hanning has been discussed, among many others, by Kristensen et al. (1992) and Kristensen (1998).

3.2 Preliminary Results

The Heimdall sodar was tested at the Risø 123 m meteorological mast. The axis of the transmitter T was vertical while that of the receiver R has an inclination of $\pi/4$ in plane of the transmitter axis and the 60 m baseline between T and R. This configuration allows the velocity component in this plane at the height 60 m. The signal is sampled in consecutive periods of $T = 1$ s where each period was digitized with the digitization period $\Delta t = T/N = 2^{-14} \simeq 6.1 \times 10^{-5}$ s, corresponding to the number $N = 2^{14}$ data points. Before the 32 bit FFT a hanning window was applied. The highest frequency, the Nyquist frequency, is $2^{13} \simeq 8.2 \times 10^3$ Hz. Using the smoothing option of the signal analyzer, the spectra, updated every second, were weighed exponentially backwards in time with a 10 s time constant. Figure 19 shows an example of a Doppler spectrum, zoomed into the interesting range. The transmitter frequency was in this case 3960 Hz which explains the pronounced narrow maximum at this frequency. The Doppler spectrum shows a narrow peak at the unavoidable transmitter frequency, which actually serves as the reference frequency, and a broad maximum. Its width is partly due to the turbulence inside the sampling volume at the intersection.

It is essential to separate the "real" Doppler spectrum due to the atmospheric

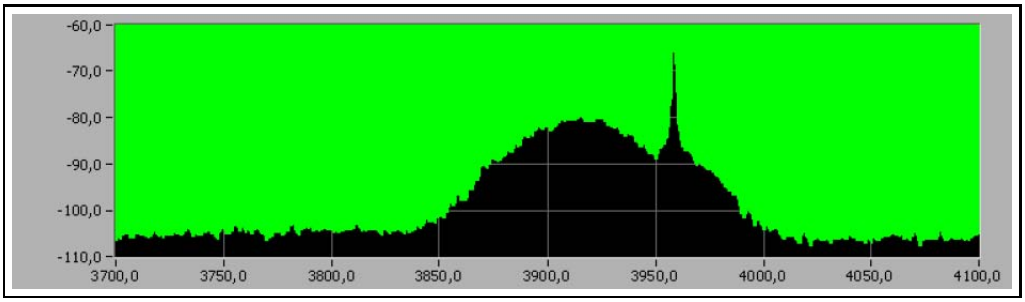

Figure 19. Doppler spectrum. The abscissa is the frequency in Hz and the ordinate the spectrum in dB units. The narrow peak at 3960 Hz is the directly transmitted frequency while the broad maximum centered at about 3910 Hz represents the velocity Doppler shift. Using (3) we find that this Doppler shift corresponds to about 6 m s^{-1}. The anemometer at the Risø mast at 60 m showed that the velocity component T-R *plane was about 5 m s^{-1}.*

scattering and the background. This background noise is large when the wind speed is high. Figure 20 shows an example of a background spectrum with no transmission from T. The wind speed is about 12–15 m $^{-1}$.

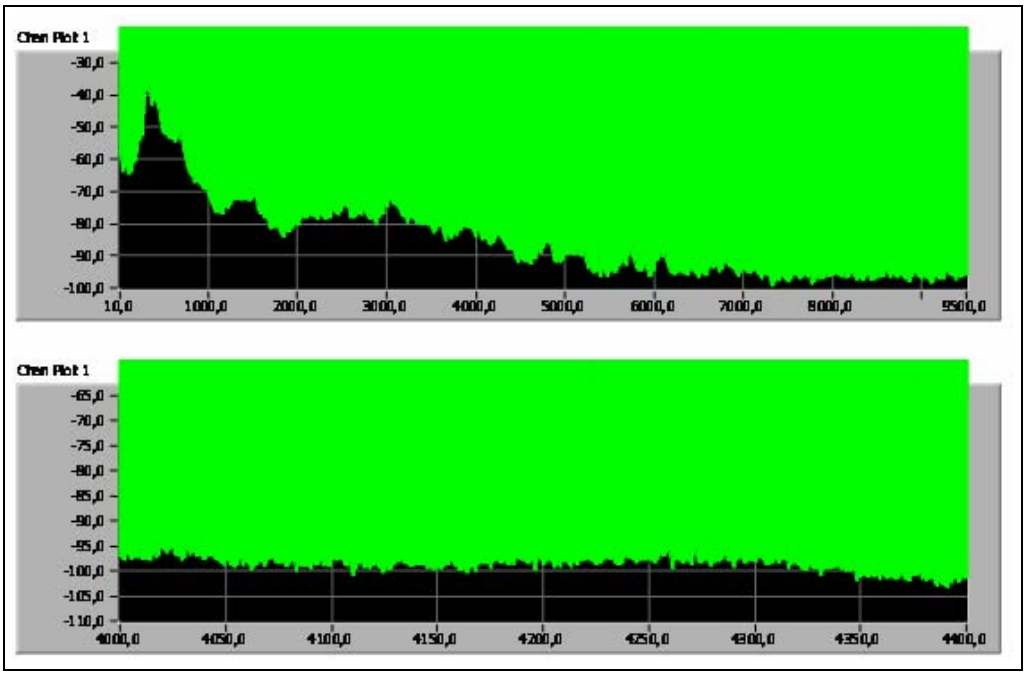

Figure 20. Noise spectra at wind speeds in the range 12–15 m^{-1}. The top frame shows the recorded spectrum and the lower frame the same spectrum, zoomed in at the important frequency range.

Another source of contamination of the Doppler spectrum are strong sidelobes from the transmitter T. Occasionally they will create scattered sound in the receiver R from another domain in space. This is illustrated in Fig. 21 and explains that there seems to be a pronounced Doppler maximum on the left side and a smaller on the right side of the reference frequency. The last is interpreted as the scattering of a transmitter sidelobe from another domain.

Figure 21 shows another example of a velocity Doppler spectrum.

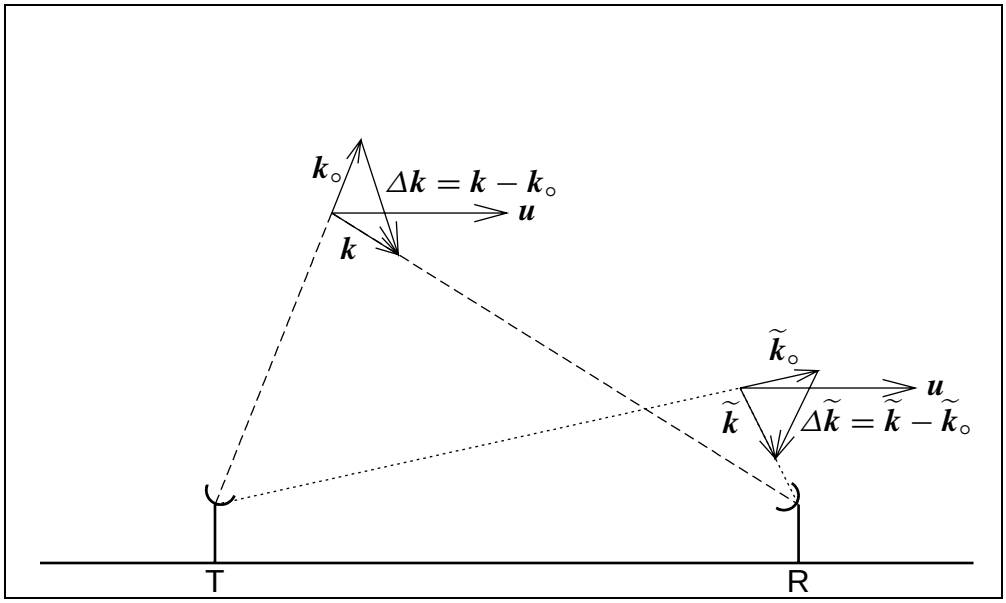

Figure 21. Scattering from the mainlobe (dashed lines) and from a sidelobe (dotted lines). The sidelobe wave-number vectors are indicated by tildes ($\tilde{\ }$). In this case the sketch shows that the two estimated velocities will have opposite sign.

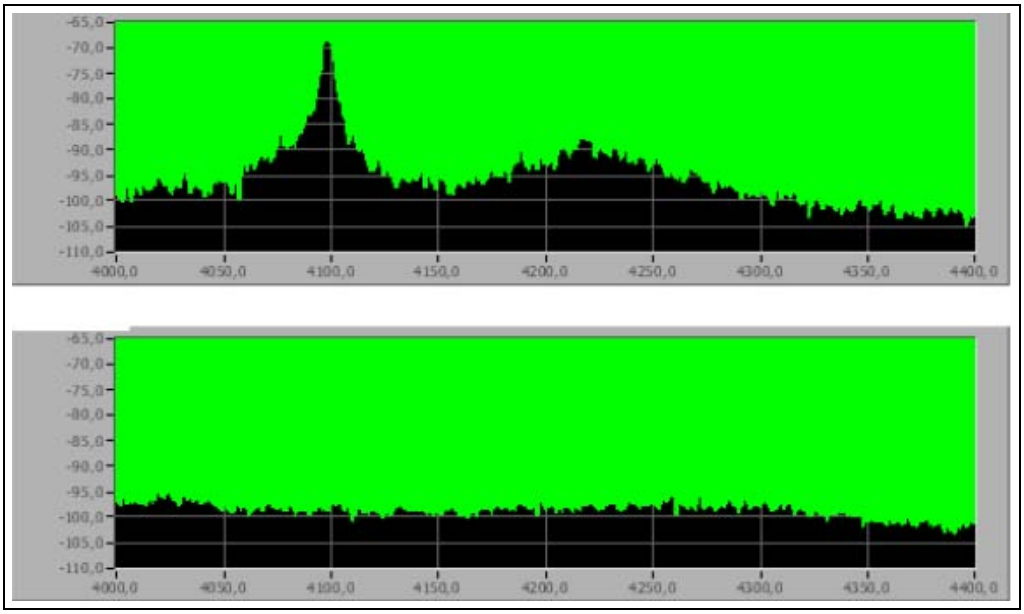

Figure 22. Instantaneous, running-mean (exponential weighted) Doppler velocity spectrum (upper frame) and corresponding noise spectrum (lower frame) at 60 m height. The broad maximum corresponds to a wind speed of 13–14 $m\,s^{-1}$. The sonic anemometer at the same height gave a 10-min average of 12 $m\,s^{-1}$, fluctuating between 6 and 16 $m\,s^{-1}$.

4 Epilogue

We have demonstrated that it is possible to obtain measurements plane projections of velocity, continuous in time, by using a bistatic sodar. The plane is defined by

the two axes of the transmitter T and the receiver R. We have tacitly assumed that this plane is vertical. However, this need not be the case. The scattering cross section (5) by Tatarskii (1967) shows that turbulent fluctuations in both temperature and velocity contribute as scattering agents. The efficiency depends on the scattering angle γ as Fig. 3 shows. Neither the velocity nor the temperature fluctuations contribute for $\gamma = 90°$ and at $\gamma = 180°$ (backscattering) the velocity fluctuations are inactive. Figure 3 indicates that we can make good use of both types of turbulent fluctuations by using $\gamma = 135°$. For a given scattering angle γ the scattering cross section is proportional to the wave-number magnitude k of the sound wave to the power 1/3 and to the structure function parameters C_V^2 and C_T^2 for the velocity fluctuations and the temperature fluctuations, respectively. These two parameters are functions of the friction velocity u_* and the heat flux H as illustrated by Figs. 5 and 6.

The Doppler velocity is obtained as a volume average, defined the the intersection between the main lobes of the directivities of the transmitter T and the receiver R. The sodar equation (58) gives the power of the received signal as a function of the position of the scattering eddy in the elliptical coordinates a, ϕ, θ. We see that the sound attenuation parameter β enters at this point. It has to be specified as a function of the surface-layer parameters T and RH and of the frequency. This is illustrated by Figs. 9–12. As we have seen, it is advantageous from a signal-strength point of view to have $\gamma = 135°$. We have determined the relative three-dimensional weighting function when T is pointing vertically and the axis of R has the inclination 45°. The three projections of this weighting function W are shown in Fig. 15.

The Heimdall sodar has not been tested thoroughly or used in operation. We have used the sodar equation to estimate the received power as a function of the transmitted power. Table 1 shows the result. The measured power is more than on order of magnitude less that the estimated power so, even considering the experimental uncertainties, this discrepancy seems unacceptable and requires a more thorough investigation. The inaccuracy of the received power does not in itself present a problem when determining Doppler shifts due to atmospheric motion. However, it is useful to be able to predict a realistic signal-to-noise ratio from the sodar equation. We have shown a few examples of measured Doppler spectra and conclude that there are three major sources of noise:

1. The receiver gets a very strong signal at the transmitter signal frequency from direct transmission. Since it is essentially monochromatic this noise can easily be identified and, in fact, be used as a reference.
2. The receiver spectrum may contain a broad maximum due to scattering of sidelobe sound. These are usually not as pronounced as the maximum due to the main lobe.
3. Strong winds create noise which is almost white in the frequency domain of interest. The noise increases with the wind speed.

The noise problems make it a challenge to construct a reliable automated system for wind speed determination which could be based on a digital technique as used here or an analogue technique like tracking of the spectral maximum by a phase-locked-loop circuit analyzer.

It has been assumed that the axes of T and R are in a vertical plane. In principle this is not necessary for bistatic sodars. The plane defined by T and R might be tilted if we want to operate a tristatic sodar system with one transmitter and

two receivers R_1 and R_2. When the planes T-R_1 and T-R_2 do not coincide it is possible to obtain two independent projection of the the wind velocity. Of course, if these planes are not vertical we must generalize the sodar equation accordingly. It seems to be worthwhile to let further investigations be concentrated on a tristatic system where the axis of T is pointing vertically and the planes T-R_1 and T-R_2 are perpendicular to each other.

Acknowledgements

This study was supported by a research grant from the Danish Technical Research Council under contract number 26-01-0086 in the period from August 2001 to December 2002. The effort by research technician Jan Nielsen in designing and constructing the Heimdall prototype acoustic parabolas and receiver horn is highly appreciated.

References

Carl, M. D., Tarbell, T. C. & Panofsky, H. A. (1973), 'Profiles of wind and temperature from towers over homogeneous terrain', *J. Atmos. Sci.* **30**, 788–794.

Frenzen, P. & Hart, L. (1983), A further note on the Kolmogorov-von Kármán product and the values of the constants, *in* 'Proc. Sixth Symp. on Turbulence and Diffusion', American Meteorological Society, Boston, MA, pp. 24–27.

Handwerker, J. (1999), *Entwicklung eines SODAR zur berührungslosen Vermessung inhomogener Windfelder*, Lehmanns, Berlin.

Kaimal, J. C. & Finnigan, J. J. (1994), *Atmospheric Boundary Layer Flows, their Structure and Measurement*, Oxford University Press, New York, Oxford.

Kristensen, L. (1978), On sodar technigues, Technical Report R-381, Risø National Laboratory.

Kristensen, L. (1998), Time series analysis, dealing with imperfect data, Technical Report I-1228(EN), Risø National Laboratory.

Kristensen, L., Coulter, R. L. & Underwood, K. H. (1978), Sodar geometry, *in* 'Proc. Fourth Symp. on Meteorological Observations and Instrumentation', American Meteorological Society, Denver, CO, pp. 391–395.

Kristensen, L., Kirkegaard, P., Fairall, C. W., Kaimal, J. C. & Lenschow, D. H. (1992), Advantages of tapering of finite data records for spectral analysis, Technical Report NOAA Technical Memorandum ERL WPL-226, National Oceaninc and Atmospheric Administration, Environtal Research Laboratories.

Kristensen, L., Lenschow, D. H., Kirkegaard, P. & Courtney, M. S. (1989), 'The spectral velocity tensor for homogeneous boundary-layer turbulence', *Boundary-Layer Meteorol.* **47**, 149–193.

Lumley, J. L. & Panofsky, H. A. (1964), *The Structure of Atmospheric Turbulence*, John Wiley & Sons, Inc., New York.

Neff, W. D. & Coulter, R. L. (1986), Acoustic remote sensing, *in* D. H. Lenschow, ed., 'Probing the Atmospheric Boundary Layer', American Meteorological Society, Boston, MA, chapter 13, pp. 201–239.

Panofsky, H. A. & Dutton, J. A. (1984), *Atmospheric Turbulence: Models and Methods for Engineering Applications*, John Wiley & Sons, Inc., New York.

Salomons, E. M. (2001), *Computational Atmospheric Acoustics*, Kluwer Academic Publishers, Dordrecht.

Tatarskii, V. I. (1967), *The Effects of the Turbulent Atmosphere on Wave Propagation*, Israel Program for Scientific Translations, Jerusalem, Israel; National Technical Information Service No. TT 68-50464, U.S. Department of Commerce, Springfield, VA.

Wilson, D. K. & Ostashev, V. E. (1998), A reexamination of acoustic scattering in the atmosphere using an improved model for the turbulence spectrum, Technical Report A375883, New Mexico State University, Las Cruces.

Risø’s research is aimed at solving concrete problems in the society.

Research targets are set through continuous dialogue with business, the political system and researchers.

The effects of our research are sustainable energy supply and new technology for the health sector.